



Porous-Media Flow Fields for Polymer Electrolyte Fuel Cells

I. Low Humidity Operation

Yun Wang^{*,z}

Renewable Energy Resources Laboratory and National Fuel Cell Research Center,
Department of Mechanical and Aerospace Engineering, The University of California, Irvine,
Irvine, California 92697-3975, USA

This paper proposes an approach of channel development for polymer electrolyte fuel cells (PEFCs), i.e., to fill porous media in the channel region, allowing a simultaneous transport of gaseous reactant, liquid, heat, and electron through the porous-media channel. The added functions of heat/electron conductivity enhance the PEFC operation and the channel design flexibility. The porous media provide support over the diffusion media, thereby diminishing the concern of contact resistance under the channel. This paper, as the first part of our work on this channel configuration, focuses on heat and electron transport, excluding liquid water impact. A theoretical analysis of the characteristics of heat transfer and electronic conduction in fuel cells and of the required pumping power for reactant flows is performed. Factors affecting the temperature variation, electronic ohmic loss, and pumping power consumption are explored. A three-dimensional model is developed, and numerical simulations are carried out to investigate the low humidity operation of fuel cells with both hollow and porous-media channel configurations. Simulation results demonstrate the enhanced characteristics of the heat and electronic current transport and the design flexibility for the proposed approach of porous-media channels.

© 2009 The Electrochemical Society. [DOI: 10.1149/1.3183781] All rights reserved.

Manuscript submitted January 9, 2009; revised manuscript received June 23, 2009. Published July 31, 2009.

Polymer electrolyte fuel cells (PEFCs), also called polymer electrolyte membrane (PEM) fuel cells, have attracted much attention recently for mobile and portable applications.¹⁻⁴ Besides their high power capability, PEM fuel cells work at low temperatures, produce water as the only by-product, and can be compactly assembled, making them one of the candidates for next-generation energy conversion devices. Different from other popular electrochemical energy devices, e.g., batteries, PEFCs generally require flow channels to deliver reactants for electrochemical reaction and remove by-product water.

Several flow fields of PEM fuel cells were developed in the past, including parallel, serpentine, pin-type, and interdigitated designs.⁵⁻⁹ The major goals of these designs is to effectively distribute the gaseous reactants for the electrochemical reactions and to facilitate water removal, e.g., the interdigitated design.⁵ In general, the flow field is grooved in bipolar plates featured by hollow channels with a cross-section dimension of ~ 1 mm.⁷ This size is not fixed but rarely increases several-fold because the gaseous reactants are poor thermal/electronic conductors. Therefore, the heat and electrons largely rely on the in-plane transport in the diffusion media (DM) for the electrochemical activity under the channel. Note that the DM may include the gas diffusion layer (GDL) and microporous layer (MPL). A large width or in-plane dimension of a channel increases the transport resistance, thereby reducing cell performance.

Heat management is a central topic in fuel cell technology because waste heat must be removed efficiently to keep the cell at its operating temperature. Exceedingly high temperatures subject the electrolyte membrane to dryness, increasing the membrane ionic resistance and hence the ohmic voltage loss. However, at low temperatures, most water exists in the liquid state due to the low water saturation pressure, and ensuing flooding may block reactant transport passages, reducing cell performance and durability. Numerous studies have been conducted to investigate the heat transfer¹⁰⁻¹⁵ within fuel cells.

Electrons are produced in the anode and conducted to the cathode via the out circuit for the oxygen reduction reaction (ORR). In most studies, the ohmic loss arising from the electronic resistance is neglected because it is typically much smaller than the membrane ionic one. This is because the electronic conductivity of fuel cell components except the membrane is several orders of magnitude

higher than the ionic one in the electrolyte membrane. Electron transport phenomena in fuel cells have been investigated in several studies.¹⁶⁻¹⁸

Despite the high thermal and electronic conductivities of the DM, heat and electron transport may encounter high resistances in this component. This may occur under the channel where the supply/removal of the heat/electrons relies on the in-plane transport in the thin DM (~ 100 μm). To diminish the transport resistances, the channel width must be sufficiently small to shorten the transport passage. A typical channel dimension is ~ 1 mm. Given that the active area of a typical industrial fuel cell is ~ 200 to 500 cm^2 ,^{7,15,19} a large number of channels, whether of parallel, serpentine, or pin-type pattern, are required, which complicates the fuel cell design and heat/water management.

In this work, we propose the idea of applying porous media to the fuel cell channel region and allowing a simultaneous transport of the fluid flow through the interconnected pores and heat/electrons via the solid matrix. This approach enhances the heat and electronic current transport in fuel cells and the flexibility of the channel design. Theoretical analysis and numerical study are conducted to compare the fuel cell performances with the proposed channel configuration and the traditional one. Low humidity operation is considered, with focus on heat and electron-transport characteristics, while the second paper in this series investigates the simultaneous flows of gas and liquid in the porous-media channel.

Mathematical Modeling and Theoretical Analysis

The submodel for fuel cell porous-media channels.—Figure 1a and b schematically shows the porous channel approach and the traditional hollow channel design. The proposed approach has porous media in its channel region, allowing a gaseous reactant transport through the interconnected pore structure. To ensure a sufficient flow conductance, highly porous media are preferred. In addition, the solid matrix must be electron and heat conductive to enable the function of allowing electron and heat transport. Common media that qualify as the channel materials include metal foams and carbon-fiber-based porous media. The porosity of metal foams can reach 98%, while that of carbon-fiber-based porous media can be fabricated over 80%. Figure 2 shows the pore structures of several typical porous media. Different from the work of Ref. 20, which introduces metal foams to replace the whole bipolar plates, the approach in this paper still keeps the ribs or land that prevent a short-cut (short circuit) of the reactant flows and consequent local reactant starvation.

* Electrochemical Society Active Member.

^z E-mail: yunw@uci.edu

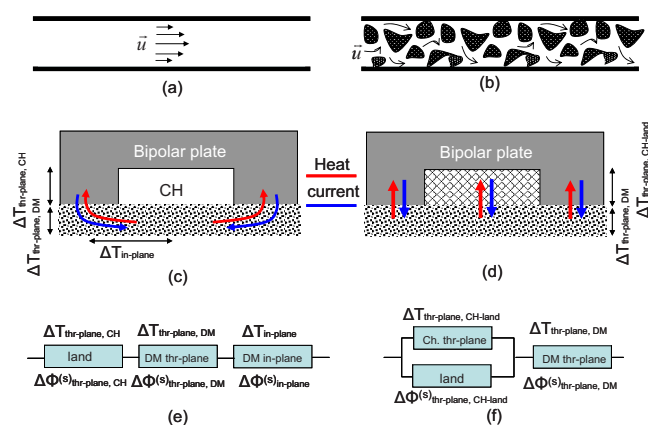


Figure 1. (Color online) Schematics of [(a) and (c)] traditional hollow channel and [(b) and (d)] proposed porous-media channel for the cathode side and their connections of thermal/electrical resistors: (e) Hollow channel and (f) porous-media channel.

In the porous-media channel with a high porosity (>0.8), the magnitude of the intrinsic velocity is comparable with the one in hollow channels of similar dimension, i.e., ~ 1 m/s. Therefore, the Reynolds number, $Re(=\rho\bar{u}_p\bar{d}/\mu)$, is ~ 1 , and the flow is in the regime of a stable laminar flow and can be well approximated by Darcy's law²¹

$$\rho\mathbf{u} = -\frac{K}{\nu}\nabla P \quad [1]$$

The above equation neglects the gravitational force due to the small pore dimension. The permeability K of porous media is related to the porosity and the mean pore radius, as approximated by the Carman-Kozeny model

$$K = \frac{\varepsilon^3}{180(1-\varepsilon)^2d^2} \quad [2]$$

Heat transport in the porous-media channel is conducted in both gas and solid phases. Assuming the local thermal equilibrium between phases holds true, the combined energy equation reads

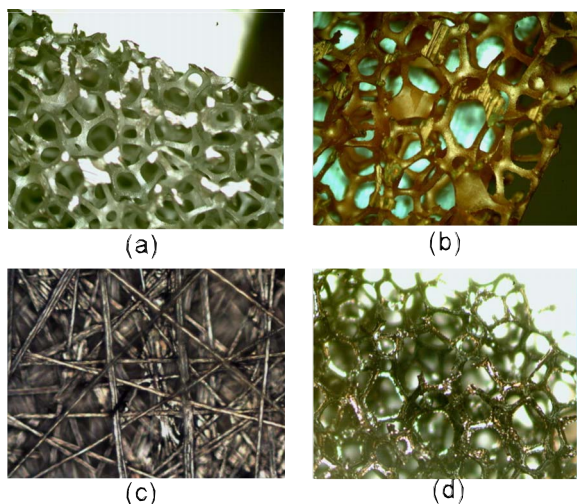


Figure 2. (Color online) Several typical porous media: (a) Al foam, (b) Cu foam, (c) C paper, and (d) C foam.

$$\begin{aligned} & \frac{\partial (\varepsilon\rho_g c_{p,g} + (1-\varepsilon)\rho_s c_{p,s})T}{\partial t} + \nabla \cdot (\rho_g c_{p,g} \mathbf{u} T) \\ & = \nabla \cdot (k^{\text{eff}} \nabla T) + \frac{i^{(s)2}}{\sigma_s^{\text{eff}}} \quad [3] \end{aligned}$$

where k^{eff} is the effective heat conductive coefficient that accounts for the contributions from solid and gaseous phases as well as the temperature spatial deviation arising from volume averaging.²¹ In general, the selected solid material is a good thermal conductor (several orders of magnitude higher than the gas); therefore, we can neglect the gaseous contribution in the conductivity k^{eff} and approximate it by the solid one modified by the Bruggeman relation. We assume that no liquid water exists in the channel, which is valid for a low humidity operation. The source term $i^{(s)2}/\sigma_s^{\text{eff}}$ arises from the electronic current resistance of the solid matrix, which is generally referred to as the Joule heating.

Electron transport in the channel solid matrix can be modeled by applying the ohmic law

$$\nabla \cdot (\sigma_s^{\text{eff}} \nabla \Phi^{(s)}) = 0 \quad [4]$$

In contrast, in traditional hollow channels, usually the Navier-Stokes equation is applied²² to describe the reactant flow. Heat transfer in the channel is dominated by the convection along the channel. The reactant gases are generally poor thermal conductors with a low volumetric heat capacity; therefore, most heat produced in the electrode is removed via the land instead of the channels. The reactant gases are non-electron conductive. Therefore, the charge equation can be excluded in the channel space. The momentum and energy equations for hollow channels are summarized as follows

$$\frac{\partial \rho_g \mathbf{u}}{\partial t} + \nabla \cdot (\rho_g \mathbf{u} \mathbf{u}) = -\nabla P + \nabla \cdot \boldsymbol{\tau} \quad [5]$$

$$\frac{\partial \rho_g c_{p,g} T}{\partial t} + \nabla \cdot (\rho_g c_{p,g} \mathbf{u} T) = \nabla \cdot (k_g \nabla T) \quad [6]$$

Model description for fuel cells.—Other components of fuel cells to be modeled include the bipolar plates, the DM, the catalyst layer, and the membrane. These components are necessary for fuel cell functions; e.g., the electrochemical reactions take place in the catalyst layer and gaseous reactants are transported to the reaction site via the DM. To develop a fuel cell model coupling the electrochemical kinetics and transport mechanisms, the following assumptions were invoked: (i) ideal gas mixtures; (ii) isotropic and homogeneous membrane, catalyst layers, DM, and channels; (iii) equilibrium between ionomer and surrounding fluid in the catalyst layer; and (iv) thermal equilibrium between phases in the porous media. The model consists of five principles of conservation: mass, momentum, energy, species, and charge. The steady-state expression can be presented as follows²³

$$\nabla \cdot \boldsymbol{\Gamma} = \mathbf{S}$$

where

$$\boldsymbol{\Gamma} = \begin{bmatrix} \mathbf{u}\rho_g \\ 0 \\ \mathbf{u}C_k + \mathbf{G}_{k,\text{diff}} \\ \mathbf{u}C_w + \mathbf{G}_{w,\text{diff}} + \frac{n_d}{F}\mathbf{i}^{(m)} \\ \rho_g c_{p,g} \mathbf{u} T - k^{\text{eff}} \nabla T \\ -\sigma_m^{\text{eff}} \nabla \Phi^{(m)} \\ -\sigma_s^{\text{eff}} \nabla \Phi^{(s)} \end{bmatrix} \quad \text{and} \quad \mathbf{S} = \begin{bmatrix} 0 \\ S_u \\ S_{C_k} \\ S_{C_w} \\ S_T \\ S_{\Phi^{(m)}} \\ S_{\Phi^{(s)}} \end{bmatrix} \quad [7]$$

where ρ , \mathbf{u} , C_k , C_w , T , $\Phi^{(m)}$, and $\Phi^{(s)}$ denote the gas density, superficial fluid velocity vector, molar concentration of reactant k , water molar concentration, temperature, electronic phase potential, and

Table I. The source terms of the conservation equations.

	S_u	S_{C_k}	S_{C_w}	S_T	$S_{\Phi(m)}/S_{\Phi(s)}$
Bipolar plates ¹⁸	—	—/—	—/—	$i^{(s)2}/\sigma_s^{\text{eff}}$	—/0
Reactant channels	$-\nabla P - \frac{\mu}{K_{\text{ch}}}\mathbf{u}$	0	0	$i^{(s)2}/\sigma_s^{\text{eff}}$	—/0
DM ^{18,23}	$-\nabla P - \frac{\mu}{K_{\text{DM}}}\mathbf{u}$	0	0	$\frac{i^{(s)2}}{\sigma_s^{\text{eff}}}$	—/0
Anode catalyst layer ^{18,23}	$-\nabla P - \frac{\mu}{K_{\text{CL}}}\mathbf{u}$	$-j/2F$	0	$j\left(\eta + T\frac{dU_o}{dT}\right)$ $+\frac{i^{(m)2}}{\sigma_m^{\text{eff}}} + i^{(s)2}/\sigma_s^{\text{eff}}$	$j/-j$
Cathode catalyst layer ^{18,23}	$-\nabla P - \frac{\mu}{K_{\text{CL}}}\mathbf{u}$	$j/4F$	$-\frac{j}{2F}$	$j\left(\eta + T\frac{dU_o}{dT}\right)$ $+\frac{i^{(m)2}}{\sigma_m^{\text{eff}}} + i^{(s)2}/\sigma_s^{\text{eff}}$	$j/-j$
Membrane ¹⁴	—	0	0	$\frac{i^{(m)2}}{\sigma_m^{\text{eff}}}$	0/—

electrolyte phase potential, respectively. The above formula also encompasses the submodel of the porous-media channel (Eq. 1 and 2) at steady state. \mathbf{G}_{diff} represents the species diffusion flux in gaseous and electrolyte phases. S_u , S_{C_k} , S_{C_w} , S_T , $S_{\Phi(m)}$, and $S_{\Phi(s)}$ are the source terms for the equations, and their expressions are summarized in Table I. The details of the source terms and necessary constitutive relations as well as the electrochemical/transport mechanisms were elaborated previously.^{14,23} In the following, the physical processes closely related to the subject of this paper are explained. *Charge transport.*—Charge production/consumption takes place at the triple-phase boundaries of the catalyst layer during the electrochemical reactions

Hydrogen oxidation reaction (HOR) in the anode:



ORR in the cathode: $\text{O}_2 + 4\text{e}^- + 4\text{H}^+ \rightarrow 2\text{H}_2\text{O} + \text{heat}$ [9]

The well-known Butler–Volmer equation can be applied to calculate the reaction rate. As the HOR is fast, a linear kinetic equation can be used, while the sluggish ORR can be approximated by the Tafel kinetics

$$\text{In the anode: } j_a = a_{0,a}^{\text{ref}} \left(\frac{C_{\text{H}_2}}{C_{\text{H}_2}^{\text{ref}}} \right)^{1/2} \left(\frac{\alpha_a + \alpha_c}{RT} F \eta \right) \quad [10]$$

$$\text{In the cathode: } j_c = -a_{0,c}^{\text{ref}} \left(\frac{C_{\text{O}_2}}{C_{\text{O}_2}^{\text{ref}}} \right) \exp\left(-\frac{\alpha_c F}{RT} \eta\right) \quad [11]$$

where the surface overpotential is defined as

$$\eta = \Phi^{(s)} - \Phi^{(m)} - U_o \quad [12]$$

Protons are produced in the anode and transport to the cathode via the membrane. The membrane ionic conductivity σ_m is dependent on the water content²⁴

$$\sigma_m = (0.5139\lambda - 0.326) \exp\left[1268\left(\frac{1}{303} - \frac{1}{T}\right)\right] \quad [13]$$

where λ denotes the membrane water content, defined as the ratio of the number of water molecules to the number of charge (SO_3H^+) sites.

The electrons are also produced in the anode and transport via the DM, bipolar plate, and out circuit to the cathode. The electronic

conductivity σ_s of the DM and bipolar plates is generally several orders of magnitude higher than σ_m in the electrolyte membrane. Therefore, the ohmic resistance due to electronic resistance is neglected in most studies. However, in several flawed designs of fuel cells, the electronic current resistance may be a limiting factor for local cell performance; for example, fuel cells that lack a sufficient contact between the DM and the membrane electrode assembly (MEA) suffer a substantial ohmic loss locally due to the large interfacial resistance. Some studies also considered the electron transport in their models.¹⁶⁻¹⁸

Heat transport.—Fuel cell operation produces waste heat. The heat sources may arise from the irreversible/reversible process of the electrochemical reaction; e.g., the transfer current overcomes the surface overpotential, the Joule heating due to the ionic/electronic current resistance, and the phase change. The first part generally contributes a major portion of heat generation, while the second is small and negligible particularly at low currents, as estimated by Wang.²⁵ Phase change releases or absorbs latent heat. It should be considered when liquid/solid water is present. At a low humidity operation, we excluded liquid/solid water and hence the phase change associated heat transfer. Wang²³ showed that flooding might occur when dry reactants were used [the inlet relative humidity (RH) in their study was $\sim 66\%$]. Neglecting the phase change, one can write the heat source as follows

$$S_T = j\left(\eta + T\frac{dU_o}{dT}\right) + \frac{i^{(m)2}}{\sigma_m^{\text{eff}}} + \frac{i^{(s)2}}{\sigma_s^{\text{eff}}} \quad [14]$$

The first term on the right side is due to the irreversible/reversible process of the reaction, while the latter two are the Joule heating. In the catalyst layer, all three terms on the right side are nonzero, while in other components only parts of the terms are nonzero; e.g., all terms vanish except $i^{(m)2}/\sigma_m^{\text{eff}}$ in the membrane region.

The materials of fuel cell components are typically very good thermal conductors, e.g., the carbon-fiber-based DM and bipolar plates. The thermal conductivity of the catalyst layer varies depending on its composition, typically 0.3–3 W/m °C.^{26,27} However, the catalyst layer is thin ($\sim 10 \mu\text{m}$) and therefore has a small through-plane temperature variation. In most of the studies on heat transfer, the temperature variation in a cross section of a fuel cell is around several degrees,^{13,14} primarily dependent on the DM material properties, channel dimension, and local current. Even such a small temperature variation can considerably affect the local water transport

as the water vapor partial pressure increases exponentially with temperature. Due to this correlation of heat and water transports, Wang and Wang¹⁵ proposed to manipulate the cooling unit to improve the characteristics of the water management. In their study, a temperature variation of $\sim 10^\circ\text{C}$ was presented inside a fuel cell.

Boundary conditions.—Equation 7 forms a complete set of governing equations with eight unknowns: \mathbf{u} (three components), P , C_k , T , $\Phi^{(m)}$, and $\Phi^{(s)}$.²³ As the single-domain description was adopted, the internal boundary conditions were satisfied automatically.

Flow inlet boundaries.—The inlet velocity \mathbf{u}_{in} in a gas channel was expressed by the respective stoichiometric flow ratio, i.e., ξ_a or ξ_c , defined at the average current density I as

$$\begin{pmatrix} \mathbf{u}_{\text{in,a}} \\ \mathbf{u}_{\text{in,c}} \end{pmatrix} \cdot \mathbf{n}|_{\text{inlet}} = -\frac{IA_m}{F} \begin{pmatrix} \frac{\xi_a}{2C_{\text{H}_2}A_a} \\ \frac{\xi_c}{4C_{\text{O}_2}A_c} \end{pmatrix} \Bigg|_{\text{inlet}} \quad [15]$$

where A_a , A_c , and A_m are the flow cross-sectional areas of the anode and cathode gas channels and the membrane area, respectively. The inlet molar concentrations were determined by the inlet pressure and humidity according to the ideal gas law.

Outlet boundaries.—Fully developed or no-flux conditions were applied.

Walls.—A no-slip and impermeable velocity condition and a no-flux condition were applied

$$\begin{aligned} \frac{\partial}{\partial n} \begin{pmatrix} \mathbf{u} \\ P \\ C_k/C_w \\ T \\ \Phi^{(m)}/\Phi^{(s)} \end{pmatrix} \Bigg|_{\text{outlet}} &= 0 \\ \mathbf{u}|_{\text{wall}} &= 0 \\ \text{and } \frac{\partial}{\partial n} \begin{pmatrix} P \\ C_k/C_w \\ \Phi^{(m)} \end{pmatrix} \Bigg|_{\text{wall}} &= 0 \end{aligned} \quad [16]$$

The boundary conditions for the electronic phase potential $\Phi^{(s)}$ and temperature at the bipolar plate outer surfaces can be expressed as

$$\begin{aligned} \begin{pmatrix} \Phi^{(s)} \\ T \end{pmatrix} \Big|_{\text{anode}} &= \begin{pmatrix} 0 \\ 353.15 \text{ K} \end{pmatrix}, \quad \begin{pmatrix} \frac{\partial \Phi^{(s)}}{\partial n} \\ T \end{pmatrix} \Bigg|_{\text{cathode}} \\ &= \begin{pmatrix} -\frac{IA_m}{\sigma_s^{\text{eff}} A_{c,\text{wall}}} \\ 353.15 \text{ K} \end{pmatrix}, \quad \text{and } \frac{\partial}{\partial n} \begin{pmatrix} \Phi^{(s)} \\ T \end{pmatrix} \Bigg|_{\text{otherwise}} = 0 \end{aligned} \quad [17]$$

where $A_{c,\text{wall}}$ is the area of the cathode outer surface.

Hollow channels vs porous-media channels.—Figure 1a and b schematically shows the traditional hollow channel design and the proposed porous-media channel, respectively, while Fig. 1c and d shows cross sections of these two designs together with DMs. To simplify the analysis, we consider a uniform current density and therefore uniform heat production and electron consumption rates.

Heat-transfer analysis.—Heat can be taken away by the reactant channel flow and cooling flow. Following Ref. 25, one can define a parameter β_1 to characterize the ratio of heat that can be removed by the reactant gas flow to the one generated by a fuel cell

$$\begin{aligned} \beta_1 &= \frac{[\rho_g c_{p,g} \Delta T A_{\text{ch}} u]_a + [\rho_g c_{p,g} \Delta T A_{\text{ch}} u]_c}{I(E_o - V_{\text{cell}})A_m} \\ &\approx \frac{\rho_{g,a} c_{p,g,a} \frac{2\xi_a}{C_{\text{H}_2}} + \rho_{g,c} c_{p,g,c} \frac{\xi_c}{C_{\text{O}_2}}}{4F(E_o - V_{\text{cell}})} \Delta T \end{aligned} \quad [18]$$

where ΔT_a and ΔT_c are the temperature increments from the inlet to the outlet on the anode and cathode sides, respectively. The last term was approximated by setting $\Delta T_a = \Delta T_c = \Delta T$. Typical values for a fuel cell, e.g., $\xi = 1.5$ and full inlet humidification, lead to $\beta_1 < 5\%$ at $\Delta T = 10 \text{ K}$, which is small and therefore can be safely neglected in the analysis. We now consider that heat is only removed by the cooling units via the bipolar plates.

(a) Traditional hollow channels. In Fig. 1c, $\Delta T_{\text{in-plane}}$ can be evaluated by assuming that the heat generation is uniformly distributed in the DM as a volumetric heat source, thereby simplifying the two-dimensional problem to a one-dimensional (1D) case

$$\Delta T_{\text{in-plane}} \approx \frac{\frac{1}{2}I(E_o - V_{\text{cell}})W_{\text{ch}}^2}{2H_{\text{DM}}k_{\text{DM},W}^{\text{eff}}} \quad [19]$$

where W_{ch} , H_{DM} , and $k_{\text{DM},W}^{\text{eff}}$ represent the in-plane characteristic length of a channel, the through-plane one of the DM, and the effective conductivity of the DM in the in-plane direction, respectively. $I(E_o - V_{\text{cell}})$ is the heat generation rate, which is removed by both anode and cathode cooling units. $\Delta T_{\text{thr-plane}}$ can be estimated by considering two thermal resistors of the DM and land connected in series, i.e., the sum of $\Delta T_{\text{thr-plane,DM}}$ and $\Delta T_{\text{thr-plane,ch}}$

$$\Delta T_{\text{thr-plane}} \approx \frac{\frac{1}{2}I(E_o - V_{\text{cell}})(W_{\text{ch}} + W_{\text{land}})/W_{\text{land}}}{\frac{k_{\text{land}}^{\text{eff}}}{H_{\text{land}}}} + \frac{\frac{1}{2}I(E_o - V_{\text{cell}})}{\frac{k_{\text{DM},H}^{\text{eff}}}{H_{\text{DM}}}} \quad [20]$$

$k_{\text{DM},H}^{\text{eff}}$ denotes the through-plane thermal conductivity, which is different from the in-plane one $k_{\text{DM},W}^{\text{eff}}$ for anisotropic DMs. For the carbon-paper DM, $k_{\text{DM},H}^{\text{eff}}$ may be an order of magnitude smaller than $k_{\text{DM},W}^{\text{eff}}$.^{28,29} The total temperature difference can then be expressed by

$$\begin{aligned} \Delta T_{\text{hollow}} &= \Delta T_{\text{in-plane}} + \Delta T_{\text{thr-plane}} \\ &= \frac{\frac{1}{2}I(E_o - V_{\text{cell}})H_{\text{DM}}}{k_{\text{DM},H}^{\text{eff}}} \left[\frac{1}{2} \left(\frac{W_{\text{ch}}}{H_{\text{DM}}} \right)^2 \frac{k_{\text{DM},H}^{\text{eff}}}{k_{\text{DM},W}^{\text{eff}}} \right. \\ &\quad \left. + \left(\frac{W_{\text{ch}}}{H_{\text{DM}}} \frac{H_{\text{DM}}}{W_{\text{land}}} + 1 \right) \frac{H_{\text{land}} k_{\text{DM},H}^{\text{eff}}}{H_{\text{DM}} k_{\text{land}}} + 1 \right] \\ &= \Delta T_{\text{DM}} f_{\text{hollow}} \left(\frac{W_{\text{ch}}}{H_{\text{DM}}}, \frac{H_{\text{DM}}}{W_{\text{land}}}, \frac{H_{\text{land}}}{H_{\text{DM}}}, \frac{k_{\text{DM},H}^{\text{eff}}}{k_{\text{DM},W}^{\text{eff}}}, \frac{k_{\text{DM},H}^{\text{eff}}}{k_{\text{land}}} \right) \end{aligned} \quad [21]$$

where $\Delta T_{\text{DM}} = [\frac{1}{2}I(E_o - V_{\text{cell}})H_{\text{DM}}]/k_{\text{DM},H}^{\text{eff}}$, and its physical meaning is the temperature drop across the DM for the 1D case. The defined function f_{hollow} combines both geometrical and thermal parameters. The typical DM materials include Toray, Sigracet, and ELAT. Their through-plane conductivities range from 0.2 to 2 W/K m,^{27,28,30} leading to $\Delta T_{\text{DM}} \sim 0.3$ to 3 K for 1.0 A/cm² and H_{DM} of 0.2 μm . Among the variables in the function f_{hollow} , the ratios of properties are generally fixed for a specific material, e.g., for the carbon paper^{28,31} and graphite bipolar plates, $k_{\text{DM},H}^{\text{eff}}/k_{\text{DM},W}^{\text{eff}}$ and $k_{\text{DM},H}^{\text{eff}}/k_{\text{land}}$ are both in the magnitude of 0.1 or less. In an automobile fuel cell stack, $H_{\text{land}}/H_{\text{DM}}$ is ~ 3 to 5 for a typical cell. The other ratios $W_{\text{ch}}/H_{\text{DM}}$ and $H_{\text{DM}}/W_{\text{land}}$ are adjustable in fuel cell design but must be kept in a range to avoid a large variation in temperature: For example, $W_{\text{ch}}/H_{\text{DM}}$ of 10 (e.g., $W_{\text{ch}} \sim 2 \text{ mm}$ and $H_{\text{DM}} \sim 0.2 \text{ mm}$) renders the first term in the bracket equal to 5, while doubling the ratio of $W_{\text{ch}}/H_{\text{DM}}$ (i.e., $W_{\text{ch}} \sim 4 \text{ mm}$) increases

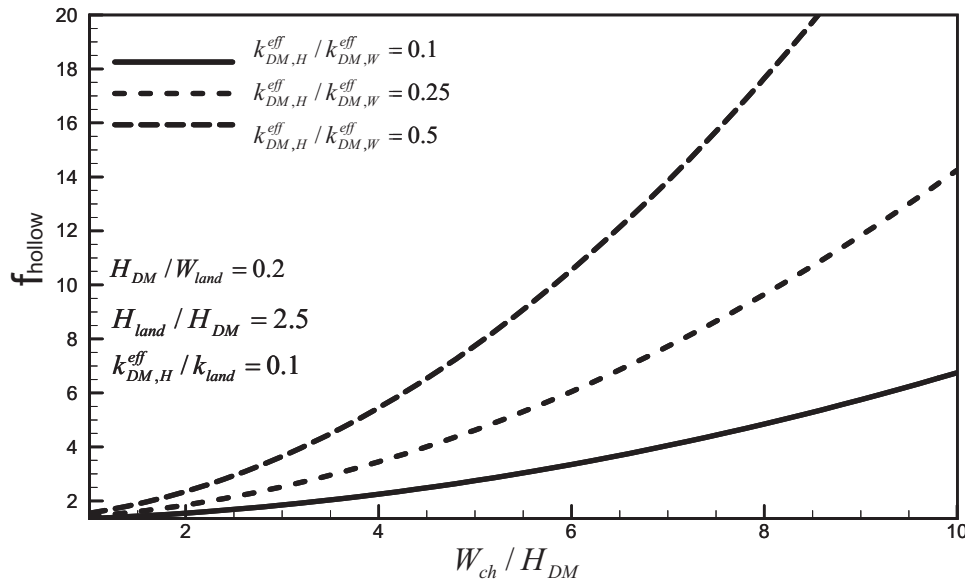


Figure 3. Profiles of f_{hollow} vs the ratio of the characteristic in-plane length of the channel to the DM thickness $W_{\text{ch}}/H_{\text{DM}}$.

the value by 4 times. Figure 3 plots the profiles of f_{hollow} vs $W_{\text{ch}}/H_{\text{DM}}$.

(b) Porous-media channel. In the porous-media channel, heat can transport through the channel directly. For a land conductivity lower than the channel's (e.g., metal foam channels), part of the heat generated under the land is also removed via the channel. Figure 1f shows the connection of the thermal resistors for the porous-media channel case. To simplify the analysis, the upper limit of the temperature difference can be estimated by only considering the thermal resistors of the DM and porous-media channel connected in series

$$\begin{aligned} \Delta T_{\text{porous}} &= \frac{\frac{1}{2}I(E_o - V_{\text{cell}})}{\frac{k_{\text{DM},H}^{\text{eff}}}{H_{\text{DM}}}} + \frac{\frac{1}{2}I(E_o - V_{\text{cell}})}{\frac{k_{\text{ch},H}^{\text{eff}}}{H_{\text{ch}}}} \\ &= \frac{\frac{1}{2}I(E_o - V_{\text{cell}})}{\frac{k_{\text{DM},H}^{\text{eff}}}{H_{\text{DM}}}} \left(1 + \frac{H_{\text{ch}} k_{\text{DM},H}^{\text{eff}}}{H_{\text{DM}} k_{\text{ch},H}^{\text{eff}}} \right) \\ &= \Delta T_{\text{DM}} f_{\text{porous}} \left(\frac{H_{\text{ch}}}{H_{\text{DM}}}, \frac{k_{\text{DM},H}^{\text{eff}}}{k_{\text{ch},H}^{\text{eff}}} \right) \end{aligned} \quad [22]$$

Note that f_{porous} contains only two ratios, $H_{\text{ch}}/H_{\text{DM}}$ and $k_{\text{DM},H}^{\text{eff}}/k_{\text{ch},H}^{\text{eff}}$, while no in-plane geometrical parameters, W_{ch} and W_{land} , are included.

Analysis of the electronic current transport.—

(a) Traditional hollow channels. As the electronic current transport follows a similar way as heat transfer, the local maximum ohmic loss can be estimated by using the same function f_{hollow} except that the thermal conductivity ratios are replaced by the electronic ones

$$\Delta \Phi_{\text{hollow}}^{(s)} = \Delta \Phi_{\text{DM}}^{(s)} f_{\text{hollow}} \left(\frac{W_{\text{ch}}}{H_{\text{DM}}}, \frac{W_{\text{ch}}}{W_{\text{land}}}, \frac{H_{\text{land}}}{H_{\text{DM}}}, \frac{\sigma_{\text{DM},H}^{\text{eff},(s)}}{\sigma_{\text{DM},W}^{\text{eff},(s)}}, \frac{\sigma_{\text{DM},H}^{\text{eff},(s)}}{\sigma_{\text{land}}^{(s)}} \right) \quad [23]$$

where $\Delta \Phi_{\text{DM}}^{(s)} = IH_{\text{DM}}/\sigma_{\text{DM},H}^{\text{eff},(s)} \sim 1$ to 10 mV given the typical values of the parameters, such as $\sigma_{\text{DM},H}^{\text{eff},(s)} \sim 200$ to 2000 s/m (Sigracet and Toray materials).

(b) Porous-media channels. Similar to Eq. 22, the upper limit of the ohmic loss can be estimated by

$$\Delta \Phi_{\text{porous}}^{(s)} = \Delta \Phi_{\text{DM}}^{(s)} f_{\text{porous}} \left(\frac{H_{\text{ch}}}{H_{\text{DM}}}, \frac{\sigma_{\text{DM},H}^{\text{eff},(s)}}{\sigma_{\text{ch},H}^{\text{eff},(s)}} \right) \quad [24]$$

Again, the function of f_{porous} is the same as the one in Eq. 22 except that the electronic conductivities are used.

Analysis of the pressure drop.— Another issue vital to fuel cells is the pressure drop through the reactant channel, which is applied to overcome the friction force exerted by the wall. This pressure drop is directly related to the pumping power consumption. As this power is an input energy to operate a fuel cell, its value affects the cell's overall efficiency.

(a) Porous-media channels. The pumping power consumption can be approximated by the product of the pressure drop along the channel and channel flow rate. The pressure drop in the channel can be estimated by Darcy's law, which directly relates the pressure gradient to the channel permeability. A parameter β_{pumping} can be defined to estimate the ratio of the pumping power for the cathode flow (the major part) to the electric power produced by a fuel cell

$$\beta_{\text{pumping}} \approx \frac{\Theta_c}{IV_{\text{cell}}A_m} \Delta P = \frac{\Theta_c}{IV_{\text{cell}}A_m} \frac{\nu \rho}{K} \mathbf{u}_c L = \frac{A_m \nu \rho L I}{16V_{\text{cell}}A_c} \left(\frac{\xi_c}{FCO_2} \right)^2 \frac{1}{K} \quad [25]$$

To ensure a small pumping power consumption or $\beta_{\text{pumping}} < 1\%$, the permeability must be over 10^{-9} m^2 given the typical values of other parameters such as $\xi_c \sim 1.5$ at 1 A/cm². By Eq. 2, the porosity of 0.9–0.95 leads to pore size $d \sim 20$ to 100 μm . In addition, the channel dimension can be changed (e.g., a smaller length L or ratio of A_m/A_c) to further relax the requirement for the porous media.

(b) Traditional hollow channels. As channel flows are generally laminar flows in PEFCs, one can define permeability, K , for the channel laminar flow through the hydraulic conductance at various cross sections. It is usually obtained, under the single-phase condition, through the well-known Hagen–Poiseuille equation

$$K = c \frac{d_h^2}{32} \quad [26]$$

where the hydraulic diameter of the channel is given by

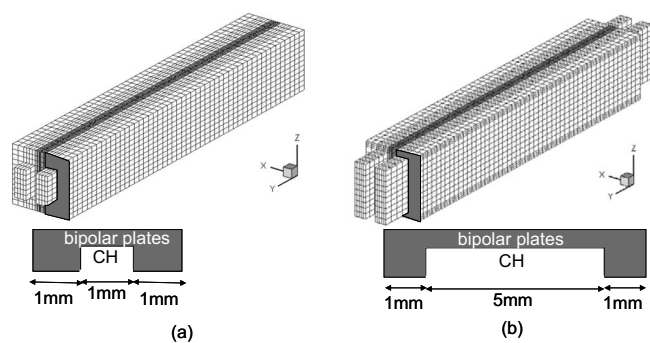


Figure 4. Geometrical and computational meshes of the two fuel cells: (a) The fuel cell with standard size (case 1); (b) the fuel cell with wider channel (case 2).

$$d_h = 4 \frac{\text{cross-section area}}{\text{channel perimeter}} \quad [27]$$

and c is called the flow shape factor, determined by the cross-section shape. The value of c for a square is 1.127, while that for a rectangle with a side length ratio of 4 is 0.874.

Given a typical square shape with a side length ~ 1 mm, the permeability is $\sim 10^{-8}$ m². Considering a stoichiometric ratio of ~ 1.5 or flow velocity of ~ 1 m/s, the pressure drop is ~ 200 Pa for the cathode. At the operating condition of 1 A/cm² and 0.6 V, $\beta_{\text{pumping}} \sim 0.1\%$.

Other issues.— Sufficient compression of the DM over the catalyst layer is crucial for the MEA's proper function. Lack of compression increases the contact resistance, and causes insufficient mechanical support that may lead to the MEA physical damage. For hollow channels, as the DM surface under the channel is free with no compression, the contact under the channel may likely be inadequate, particularly considering that the DM may be subject to deformation upon the land compression, i.e., the DM extrusion into the channel. As to the proposed approach, the porous media in the channel imposes a pressure over the DM. The pressure can also be adjusted by selecting proper solid materials or compression of the channel porous media.

Numerical procedures.— The governing equations, Eq. 7, along with their appropriate boundary conditions were discretized by the finite volume method and solved by a commercial flow solver, Fluent (version 6.0.12), using the SIMPLE (semi-implicit pressure linked equation) algorithm.³² The SIMPLE algorithm updates the pressure and velocity fields from the solution of a pressure correction equation solved by the algebraic multigrid method. Following

the solution of the flow field, species equations were solved. The source terms and physical properties were implemented in a user-defined function, and the species transport equations were solved through the software's user-defined scalars. The computational domains in the numerical studies are shown in Fig. 4. Geometrical and operating parameters are listed in Table II. Approximately 60,000 ($60 \times 100 \times 10$) and $\sim 120,000$ ($60 \times 100 \times 20$) computational cells were used to capture the electrochemically coupled transport phenomena within fuel cells. Overall species balance is checked in addition to the equation residuals as important convergence criteria. These species balance checks also ensure physically meaningful results. In all the simulations presented in the next section, values of species imbalance are all less than 1%, and equation residuals are smaller than 10^{-6} .

Results and Discussion

To demonstrate the advantages of the proposed approach, PEFCs with the hollow and porous-media channels were considered in the following numerical simulations for comparison. Two sizes of PEFC channels were selected: One is the typical geometrical dimension (denoted as case 1); i.e., the ratio of the channel width to the DM thickness is 5 (typically, the channel width is ~ 1 mm and the DM thickness is ~ 0.2 mm). The other (denoted as case 2) has a wider channel (ratio ~ 25 ; see Fig. 4). Two external humidifications were considered: Case 1 works under RH = 25%/25%, while the other works under RH = 42%/42%.

Figure 5 displays the predictions of fuel cell performance. For case 1, the two polarization curves are close in the region of the current < 1.0 A/cm², and distinction appears at high current density, while for case 2 the difference is remarkable even at low currents, with porous-media channels showing a better performance. To explore the fundamental reasons for the difference observed, we chose three sets of operating conditions for a detailed investigation. Table III compares the performances of the two channel approaches at the three conditions.

Figure 6 shows the electronic phase potential distribution in the cathode at the midsection of the fuel cell. The anode one follows a similar pattern of contours except that the gradient reverses, and is therefore excluded from this figure. For case 1, there exists an observable drop in electronic phase potential (~ 10 mV) from the underchannel region to the bipolar plate in the hollow channel fuel cell, while the variation in the porous-media channel is much smaller, ~ 2 mV. This is because electrons can be conducted directly through the porous-media channel, while the hollow channel is nonconductive. Therefore, the electronic current under the channel is forced to transport in the in-plane direction in the thin DM. For the wider channel, i.e., case 2, the variation is greatly enlarged for the hollow channel fuel cell, as shown in (b) and (c) where ~ 50 mV ohmic losses are indicated. The reason is that the elec-

Table II. Geometrical, physical, and operating parameters.

Quantity	Value
Gas channel depth/width	0.5/1.0 or 5 mm
Shoulder width	1.0 mm
GDL/catalyst layer/Membrane thickness, δ	0.2/0.01/0.03 mm
Anode/cathode pressures, P	2.0/2.0 atm
Stoichiometry, ξ_a/ξ_c at 1.0 A cm ⁻²	1.5/2.0
Porosity of GDLs/catalyst layers, ε ²³	0.6/0.4
Volume fraction of ionomer in catalyst layers, ε_m ²³	0.2
Tortuosity, τ_d/τ_m ³¹	1.5/1.5
Electronic conductivity of DM/ch/bipolar plate, σ_s^{eff} ^{18,23}	500/500/2000 W m ⁻¹ K ⁻¹
Thermal conductivity, $k_m^{\text{eff}}/k_{\text{CL}}^{\text{eff}}/k_{\text{DM}}^{\text{eff}}/k_{\text{land}}^{\text{eff}}/k_{\text{ch}}^{\text{eff}}$ ¹⁴	0.95/3.0/3.0/20.0/3.0 W/m K
Permeability of DM/ch, $K_{\text{DM}}/K_{\text{ch}}$	$10^{-12}/3 \times 10^{-9}$ m ²
Exchange current density \times reaction surface area, $a_0 i_{0,a}/a_0 i_{0,c}$ ²³	$1.0 \times 10^9/1.0 \times 10^4$ A m ⁻³
Species diffusivity in anode gas at standard condition, $D_{\text{o},\text{H}_2/w}$ ²³	$1.1/1.1 \times 10^{-4}$ m ² s ⁻¹
Species diffusivity in cathode gas at standard condition, $D_{\text{o},\text{O}_2/w}$ ²³	$3.24/3.89 \times 10^{-5}$ m ² s ⁻¹

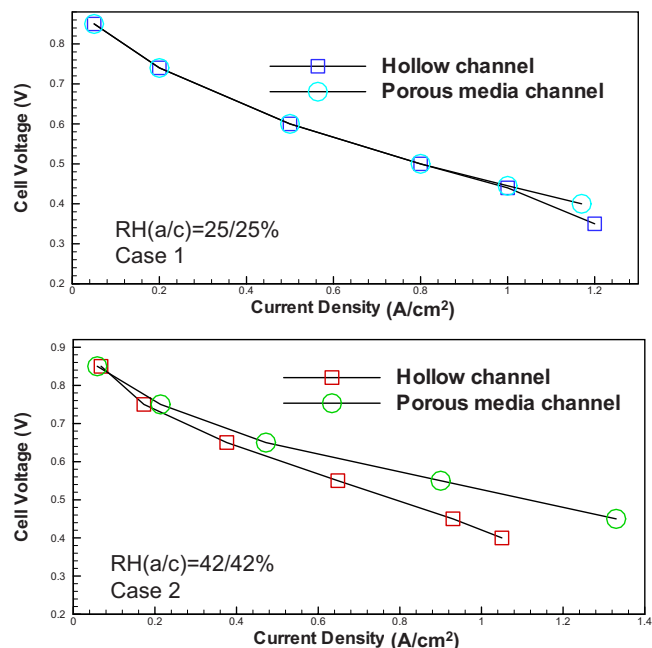


Figure 5. (Color online) Polarization curves of PEFCs for both cases.

Table III. Comparison of fuel cells with the two channel configurations.

	Hollow channel	Porous-media channel
Case 1 (RH = 26%/26%)	0.35 V at 1.2 A/cm ²	0.39 V at 1.2 A/cm ²
Case 2 (RH = 42%/42%)	0.605 V at 0.5 A/cm ² 0.42 V at 1.0 A/cm ²	0.641 V at 0.5 A/cm ² 0.53 V at 1.0 A/cm ²

tronic current in the DM encounters a much larger in-plane resistance. However, for the porous-media channel, the electronic potential variation remains as small as case 1 as electrons are able to conduct through the channel region. This is also consistent with the theoretical analysis by Eq. 24.

Figure 7 shows the temperature distributions at the midsection of the fuel cell. Though the cathode side contributes the major heat source due to the larger surface overpotential, the temperature profile is almost symmetric as the membrane thermal resistance is low due to its small thickness. Though heat can be taken away from the reactant flows, its contribution only accounts for a small portion of the heat generation, as estimated by Eq. 18. Therefore, for the PEFC with the hollow channel, heat transport in the DM is similar with the electrons; i.e., under the channel region the in-plane transport dominates. For case 2 where the channel width is much larger, ~ 6 and ~ 2 K temperature changes are observed for high and low currents, respectively. As the porous-media channel, due to its capability for efficient conductivity, the temperature variations are much smaller, < 1.5 K, for both cases. Further, the thermal conductivity of the porous media may be higher than the bipolar plate, e.g., metal foams. In that case, a higher temperature appears under the land.

Figure 8 shows the temperature distributions in the midplane of the membrane. Though the trends are similar between the two channel configurations, i.e., a higher temperature appears near the outlet, the scales are quite different, with the ones of the hollow channel fuel cell much higher than the porous-media one at high currents, while almost the same at low current. The difference between the two channel configurations is evident under the channel. Despite the only several degree difference, the higher temperature for the hollow channel case may substantially increase the degree of membrane dryness as the vapor saturation pressure is sensitive to temperature. Also, higher temperatures benefit local electrochemical kinetics and transport processes.

Figure 9 displays the water content in the midplane of the membrane. The fuel cells with hollow channels always exhibit drier membranes than the ones with porous-media ones, particularly for the geometry with a wider channel. This is attributed to the higher temperatures in the fuel cells with hollow channels (see Fig. 8). As

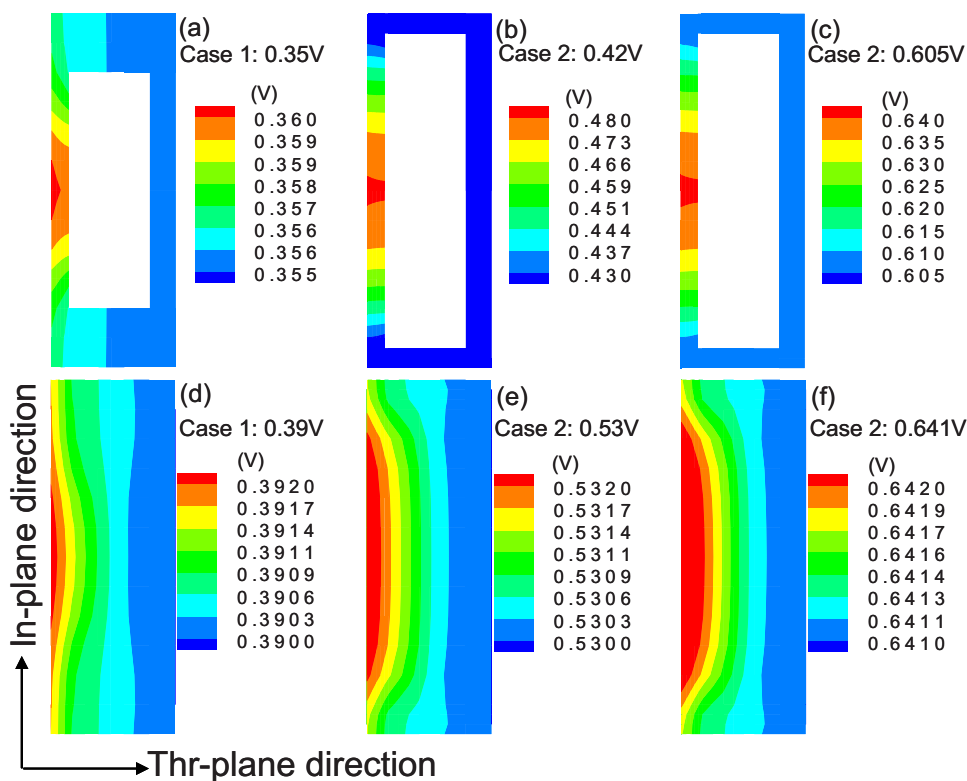


Figure 6. (Color online) Electronic phase potential distribution in the cathode at the midsection of the fuel cell. [(a)–(c)] Hollow channel and [(d)–(f)] porous-media channel. The in-plane scales are different between cases 1 and 2.

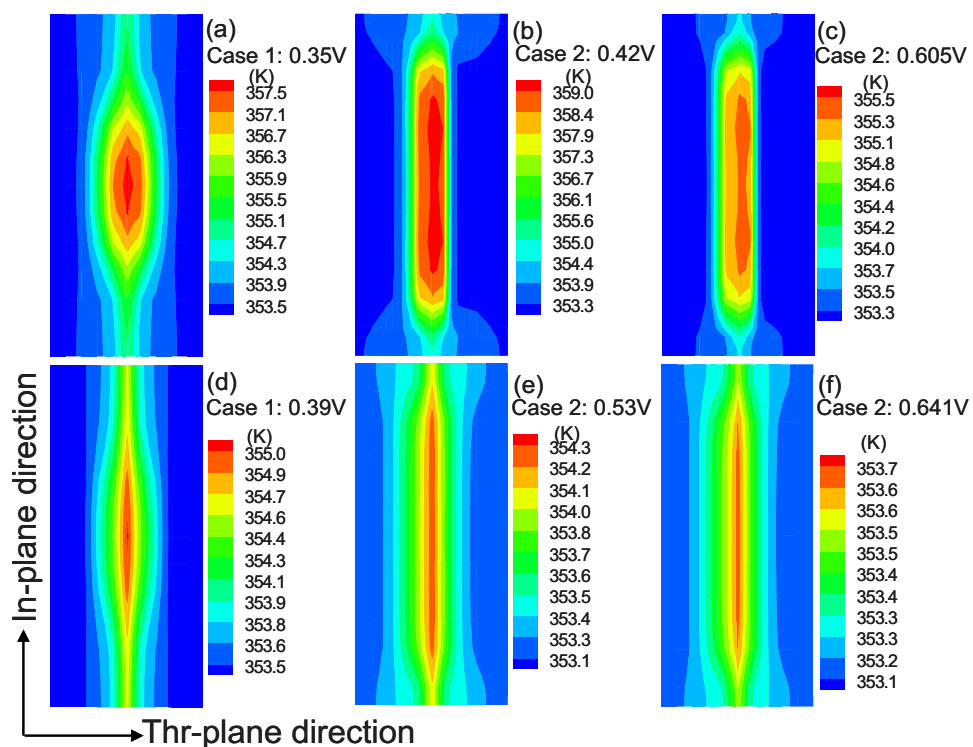


Figure 7. (Color online) The temperature distribution in the midsection of fuel cells. [(a)–(c)] Hollow channel and [(d)–(f)] porous-media channel. The in-plane scales are different between cases 1 and 2.

shown in Eq. 13, the ionic conductivity increases linearly with the water content. Therefore, the porous-media-channel fuel cell encounters a lower ionic resistance in its membrane.

Figure 10 shows the current density distribution in the midplane of the membrane. For the standard geometry, i.e., case 1, the current densities follow a similar pattern: Low currents appear near the inlet due to the dry injection, while near the outlet the current densities become higher under the channel due to water addition from the reaction. Also near the outlet, a higher current under the channel

leads to a severe mass-transport limitation, and hence a low current density is shown under the land. However, for case 2 the pattern changes. For hollow channels, lower current appears in the channel region. The current increases when approaching the land due to the smaller electron and heat transport resistances. At the high current, i.e., Fig. 10b, the local current drops again in the land downstream as the mass-transport limitation becomes dominant, while at the low current, i.e., Fig. 10c, the ohmic mechanism always dominates. Therefore, a high current appears under the land. In contrast, the

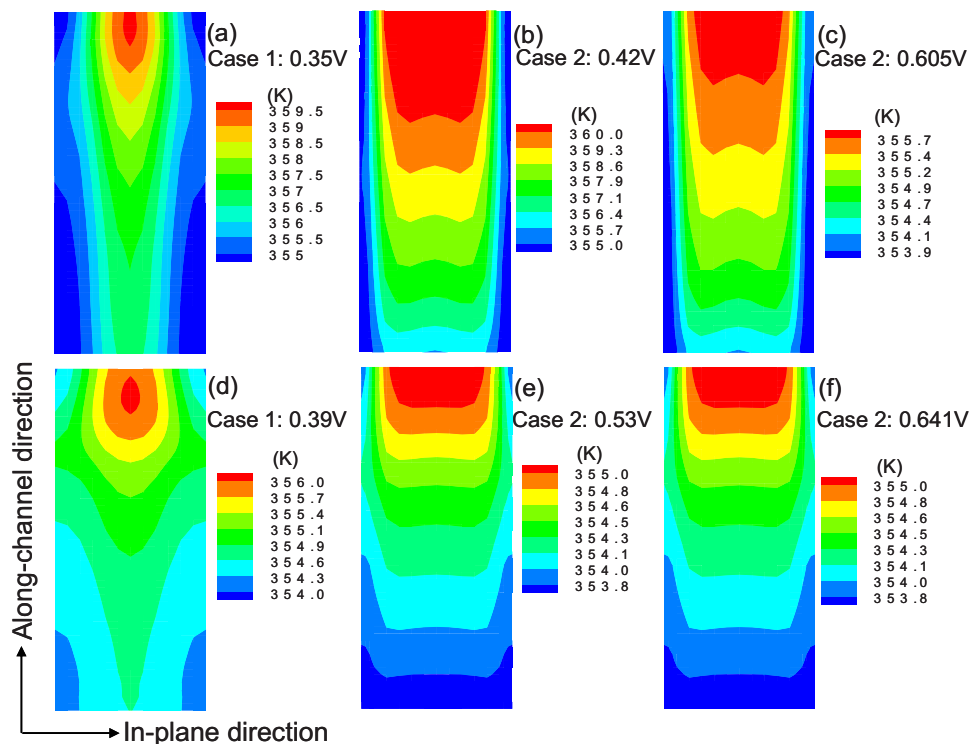


Figure 8. (Color online) Temperature distributions in the midplane of the membrane. [(a)–(c)] Hollow channel and [(d)–(f)] porous-media channel. The in-plane scales are different between cases 1 and 2.

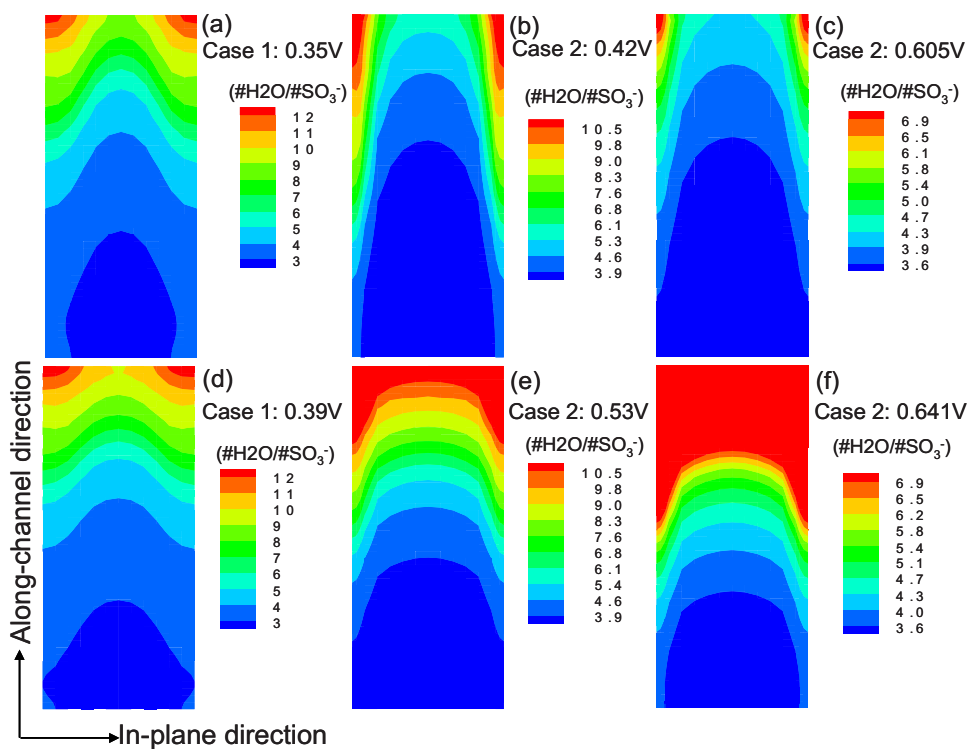


Figure 9. (Color online) Water content distributions in the midplane of the membrane. [(a)–(c)] Hollow channel and [(d)–(f)] porous-media channel. The in-plane scales are different between cases 1 and 2.

porous-media channel follows the trend of case 1 because heat removal and electronic ohmic loss under the channel are not a concern any more, and their impacts on the local cell performance can be neglected. The local performance is solely governed by the combination of two major mechanisms, i.e., membrane hydration level and mass-transport limitation. The former leads to a high current near the outlet as water addition reduces the ionic resistance along the flow, while the latter affects the cell performance primarily under the land at a high current (see Fig. 10e).

The selection of high conductivity materials such as the DM relaxes the channel dimension requirement for hollow channels, as indicated by Eq. 21. For example, choosing metal foams as DM materials may lead to a comparable result between the two configurations considered in this paper. However, issues such as the increased contact resistance or lack of mechanical support are still a concern. For the porous-media channel, the resistance is independent of channel dimension as the channel porous media provide

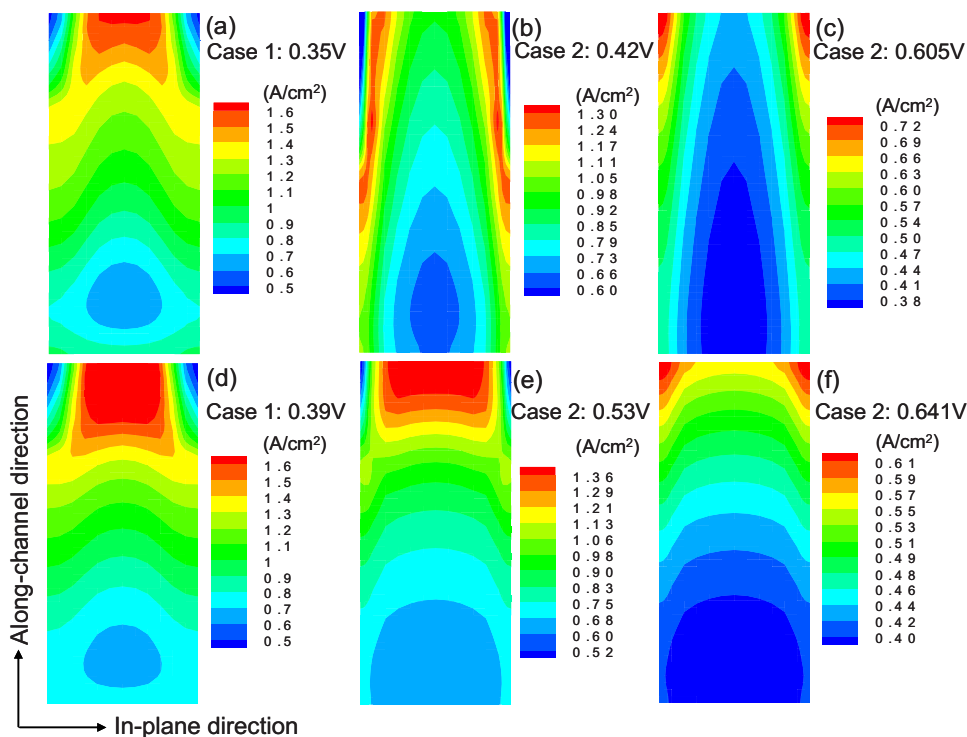


Figure 10. (Color online) The current density distribution in the midplane of the membrane. [(a)–(c)] Hollow channel and [(d)–(f)] porous-media channel. The in-plane scales are different between cases 1 and 2.

support over the DM. Further, even with better conductive DMs, there still exists a limit for the channel width, as indicated by Eq. 21.

Conclusions

In this work, we proposed an approach for PEM fuel cell channels, i.e., applying porous media to the channel space, allowing the transport of gaseous reactants and heat/electrons through the channel via a void space and a solid matrix, respectively. Theoretical analyses were performed to evaluate the local temperature variation, ohmic loss, and pumping power for both hollow channel and porous-media-channel fuel cells. Analyses indicated that the in-plane channel dimension and DM thermal property have negligible impacts on the local temperature variation and electronic ohmic loss for the proposed channel design but are crucial for the ones in the hollow channel fuel cell. A mathematical model was developed to couple the reactant flow, heat transfer, species transport, and electrochemical kinetics in the fuel cell. Three-dimensional simulations were carried out on two different channel in-plane dimensions. Simulations indicated that the fuel cells with a standard dimension show similar performances at low and intermediate currents for both channel configurations, while the wider-channel cases indicated distinct performances, with the porous-media channel design being superior. Detailed contours of important quantities revealed that the porous-media channels improve the characteristics of heat/electron transport in the fuel cell, thereby improving the fuel cell performance.

Acknowledgments

Partial support of this work by the Academic Senate Council on Research, Computing and Library Resources and the High Performance Computing (MPC) program at UCI is gratefully acknowledged. The author also thanks Kevin Ni from Whitney High School, Cerritos, CA, for help with the porous media pictures.

The University of California, Irvine assisted in meeting the publication costs of this article.

List of Symbols

A	area, m ²
c	flow shape factor
C	molar concentration, mol/m ³
$c_{p,g}$	specific heat, J/kg K
d	diameter, m
D	mass diffusivity of species, m ² /s
F	Faraday's constant, 96,487 C/equivalent
H	height, m
i_e	superficial current density, A cm ⁻²
I	current density, A/cm ²
k	thermal conductivity, W/m K
k_r	relative permeability
K	permeability, m ²
L	length, m
M	molecular weight, kg/mol
n	direction normal to the surface
P	pressure, Pa
R	gas constant, 8.134 J/mol K
S	source term in transport equations
t	time, s
T	temperature, K
\mathbf{u}	velocity vector, m/s
W	width, m

Greek

α	transfer coefficient
ε	porosity
η	surface overpotential, V
Θ	volumetric flow ratio, m ³ /s
ν	kinematic viscosity, m ² /s
ξ	stoichiometric flow ratio
ρ	density, kg/m ³
σ	surface tension, N/m; conductivity, S/m
τ	tortuosity factor
Φ	phase potential, V

Superscripts and subscripts

a	anode
c	cathode
eff	effective value
g	gas
h	hydraulic
H	through-plane dimension
in	inlet
k	species
m	membrane
o	standard condition
s	solid
sat	saturated value
W	width or in-plane dimension

References

1. M. L. Perry and T. F. Fuller, *J. Electrochem. Soc.*, **149**, S59 (2002).
2. C. Y. Wang, *Chem. Rev. (Washington, D.C.)*, **104**, 4727 (2004).
3. P. Costamagna and S. Srinivasan, *J. Power Sources*, **102**, 242 (2001).
4. P. Costamagna and S. Srinivasan, *J. Power Sources*, **102**, 253 (2001).
5. T. V. Nguyen and W. He, in *Handbook of Fuel Cells: Fundamentals, Technology and Applications*, W. Vielstich, H. Gasteiger, and A. Lamm, Editors, Vol. 3, Chap. 28, John Wiley & Sons, New York (2003).
6. T. V. Nguyen, *J. Electrochem. Soc.*, **143**, L103 (1996).
7. D. P. Wilkison and O. Vanderleeden, in *Handbook of Fuel Cells: Fundamentals, Technology and Applications*, W. Vielstich, H. Gasteiger, and A. Lamm, Editors, Vol. 3, Chap. 27, John Wiley & Sons, New York (2003).
8. X. Li and I. Sabir, *Int. J. Hydrogen Energy*, **30**, 359 (2005).
9. Y. Wang and C. Y. Wang, *J. Power Sources*, **147**, 148 (2005).
10. G. Maggio, V. Recupero, and C. Mantegazza, *J. Power Sources*, **62**, 167 (1996).
11. S. Mazumder and J. V. Cole, *J. Electrochem. Soc.*, **150**, A1503 (2003).
12. T. F. Fuller and J. Newman, *J. Electrochem. Soc.*, **140**, 1218 (1993).
13. H. Ju, H. Meng, and C. Y. Wang, *Int. J. Heat Mass Transfer*, **48**, 1303 (2005).
14. Y. Wang and C. Y. Wang, *J. Electrochem. Soc.*, **153**, A1193 (2006).
15. Y. Wang and C. Y. Wang, *J. Power Sources*, **153**, 130 (2006).
16. D. M. Bernardi and M. W. Verbrugge, *AIChE J.*, **37**, 1151 (1991).
17. D. M. Bernardi and M. W. Verbrugge, *J. Electrochem. Soc.*, **139**, 2477 (1992).
18. H. Meng and C. Y. Wang, *J. Electrochem. Soc.*, **151**, A358 (2004).
19. S. Shimpalee, S. Greenway, D. Spuckler, and J. W. Van Zee, *J. Power Sources*, **135**, 79 (2004).
20. S. Arisetty, A. K. Prasad, and S. G. Advani, *J. Power Sources*, **165**, 49 (2007).
21. M. Kaviaty, *Principles of Heat Transfer in Porous Media*, 2nd ed., Springer, New York (1999).
22. Y. Wang and C. Y. Wang, *J. Electrochem. Soc.*, **152**, A445 (2005).
23. Y. Wang, *J. Power Sources*, **185**, 261 (2008).
24. T. E. Springer, T. A. Zawodinski, and S. Gottesfeld, *J. Electrochem. Soc.*, **138**, 2334 (1991).
25. Y. Wang, *J. Electrochem. Soc.*, **154**, B1041 (2007).
26. Y. Wang and X. Feng, *J. Electrochem. Soc.*, **155**, B1289 (2008).
27. Y. Wang and X. Feng, *J. Electrochem. Soc.*, **156**, B1134 (2009).
28. M. Mathias, J. Roth, J. Fleming, and W. Lehnert, in *Handbook of Fuel Cells: Fundamentals, Technology and Applications*, W. Vielstich, H. Gasteiger, and A. Lamm, Editors, Vol. 3, John Wiley & Sons, New York (2003).
29. H. Meng, *J. Power Sources*, **161**, 466 (2006).
30. M. Khandelwal and M. M. Mench, *J. Power Sources*, **161**, 1106 (2006).
31. Y. Wang, C. Y. Wang, and K. S. Chen, *Electrochim. Acta*, **52**, 3965 (2007).
32. S. V. Patankar, *Numerical Heat Transfer and Fluid Flow*, Hemisphere, New York (1980).